SIAM J. APPL. MATH.
Vol. 69, No. 3, pp. 769–786
© 2008 Society for Industrial and Applied Mathematics

STEADY AND INTERMITTENT SLIPPING IN A MODEL OF LANDSLIDE MOTION REGULATED BY PORE-PRESSURE FEEDBACK*

DAVID G. SCHAEFFER† AND RICHARD M. IVERSON‡

Abstract. This paper studies a parsimonious model of landslide motion, which consists of the one-dimensional diffusion equation (for pore pressure) coupled through a boundary condition to a first-order ODE (Newton's second law). Velocity weakening of sliding friction gives rise to nonlinearity in the model. Analysis shows that solutions of the model equations exhibit a subcritical Hopf bifurcation in which stable, steady sliding can transition to cyclical, stick-slip motion. Numerical computations confirm the analytical predictions of the parameter values at which bifurcation occurs. The existence of stick-slip behavior in part of the parameter space is particularly noteworthy because, *unlike stick-slip behavior in classical models*, here it arises in the absence of a reversible (elastic) driving force. Instead, the driving force is static (gravitational), mediated by the effects of pore-pressure diffusion on frictional resistance.

Key words. Hopf bifurcation, landslide, pore pressure, stick-slip

AMS subject classifications. 74H60, 74F10, 74C99, 37G15

DOI. 10.1137/07070704X

1. Introduction.

Landslides exhibit a great diversity of movement styles and rates, including steady creeping slip, intermittent rapid slip, and catastrophic avalanching. Recently Iverson [4, 5] introduced a new theoretical model that in numerical simulations exhibits all these behaviors as a consequence of pore-pressure feedback. Most intriguing is the transition between steady and intermittent slip. In this paper we analyze this transition as a bifurcation problem.

As sketched in Figure 2.1, consider a block of porous soil on a rigid planar slope that is inclined at an angle θ. If there is no liquid in the pores of the soil, then friction can support its weight at rest provided μ_0, the coefficient of static friction, is greater than $\tan\theta$. If, however, water pressure acting on the base of the block is sufficiently large, the block will begin to slide. Suppose that it slides rigidly except for a zone of intense shearing at its base. If the soil in the basal shear zone is compacted, the governing equations admit a solution with steady sliding, due to the following sequence of physical effects:

> As the basal zone shears, it dilates; this expansion creates new pore space, thereby reducing the fluid pressure in the expanding pores; in consequence, the normal traction on the soil matrix is increased; and increased friction between the soil and the base can balance the driving and resisting forces, leading to steady creep as water pressure is restored by steady diffusion from the overlying slide block.

If friction is rate-independent, this steady creeping motion is stable. However, even a small amount of rate softening in the friction law is sufficient to destabilize steady

*Received by the editors October 31, 2007; accepted for publication (in revised form) August 5, 2008; published electronically December 19, 2008.
http://www.siam.org/journals/siap/69-3/70704.html
†Math Dept., Duke University, Durham, NC 27708 (dgs@math.duke.edu). The research of this author was supported under NSF grant DMS-0244492.
‡U.S. Geological Survey, Cascades Volcano Observatory, Vancouver, WA 98686 (riverson@usgs.gov).

motion through a Hopf bifurcation. This bifurcation is the primary focus of the present paper.

Hopf bifurcation explains the origin of oscillatory behavior in the system. Intermittent behavior—brief periods of rapid slipping alternating with comparatively long periods with no slipping—arises from the singular behavior of friction at zero velocity. Specifically, the resisting frictional force jumps to a static value dictated by the ambient pore pressure. The block then remains stationary while diffusion brings pore pressure back up to a level where friction can no longer balance gravity.

The outline of this paper is as follows. In section 2 we introduce the equations of Iverson's model, nondimensionalize them, and linearize them around the steady-state solution. Mathematically, provided the block velocity is positive, this model may be described as a parabolic PDE for the pore pressure coupled through a boundary condition to an ODE for the block velocity. In section 3 the linearized equations are solved by separation of variables, leading to a trancendental equation for eigenvalues. In section 4 we extract the condition for bifurcation by analyzing the eigenvalue equation. In section 5 we summarize the results of supporting computations, which agree well with the theoretical predictions. In section 6 we present a concluding discussion regarding our findings. Finally, in an appendix we provide a mathematical proof omitted from the main text.

Mathematically, this model is interesting in that time-periodic behavior appears in a problem governed by the (scalar) diffusion equation (of course, coupled to an ODE through a boundary condition). Physically, the model is important because it provides a parsimonious mathematical description of diverse landslide behavior that has not been rigorously analyzed until now.

2. Governing equations.

2.1. Dimensional formulation. As indicated in Figure 2.1, consider a block of soil of porosity ϕ, height H_s, and density ρ_s, which is defined as the mass of solid grains per unit total volume (i.e., the porosity is factored into ρ_s). The block is saturated with pore water of density ρ_w to a height H_w that does not change with time.[1]

Suppose this system is supported by a planar slope inclined at an angle θ. Using coordinates aligned with the slope, we describe this system by the pore pressure $p(y,t)$, the traction $\tau_x(t), \tau_y(t)$ exerted by the supporting plane on the solid matrix (effective stress at the base), and, assuming the block slides as a rigid unit over a shearing basal zone, the velocity $v_x(t), v_y(t)$ of the block. The motion is assumed to be one-dimensional in that all variables are independent of the tangential coordinate x, but it is two-dimensional in that the block is allowed to move in the normal direction as well as the tangential—indeed, dilatancy of the shearing basal zone requires this.

Let us decompose the total pore pressure into a hydrostatic component plus the excess pore pressure associated with dilation,

$$p_{\text{tot}}(y,t) = p_{\text{hydro}}(y) + p_{\text{ex}}(y,t),$$

[1]The assumption that H_w is constant is not strictly satisfied owing to small fluxes of water to and from the basal shear zone. Changes in H_w can be estimated from simple mass-balance considerations. On this basis we estimate that such changes are less than 1%. We exclude such changes from our model, however, not only for the sake of simplicity, but also because rigorous assessment of changes in water-table height requires consideration of hysteretic, nonlinear processes associated with variably saturated groundwater flow [2].

Incidentally, the model can easily be modified to allow for flux of water into the soil beneath the shear zone as well as flux into the soil above the shear zone. Computations with these options did not differ qualitatively from those reported here.

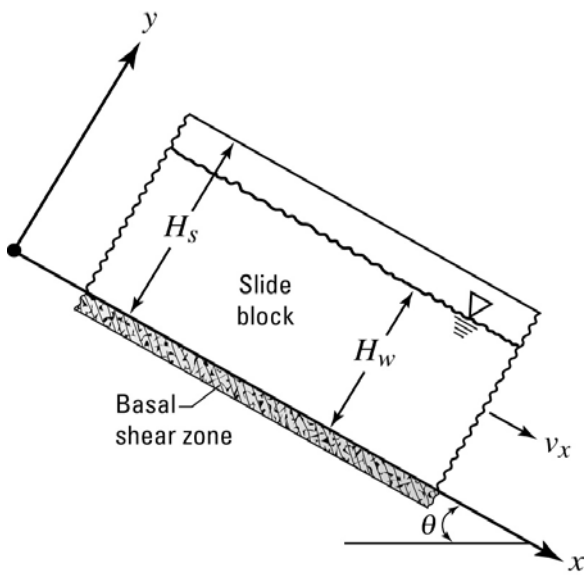

FIG. 2.1. *Schematic of landslide block.*

where

$$p_{\text{hydro}}(y) = \rho_w g \cos\theta (H_w - y). \tag{2.1}$$

Following arguments summarized by Iverson [5], we suppose the excess pore pressure evolves diffusively,

$$\partial_t p_{\text{ex}} = D \partial_{yy} p_{\text{ex}}, \qquad 0 < y < H_w, \tag{2.2}$$

with boundary conditions

$$\begin{array}{lrcl} \text{(a)} & p_{\text{ex}}(H_w, t) & = & 0, \\ \text{(b)} & \partial_y p_{\text{ex}}(0, t) & = & (\rho_w g / K) v_y(t), \end{array} \tag{2.3}$$

where D is the saturated hydraulic diffusivity, K is the saturated hydraulic conductivity below the water table, and g is the acceleration of gravity. Typical values for these parameters, and for others below, are given in Table 2.1. Equation (2.3)(b) follows from Darcy's law [2]: the excess-pressure gradient at the boundary of the shear zone is proportional to the fluid flux through the boundary that is needed to fill the volume vacated through dilatancy.

In Iverson's model, the behavior of the basal zone is characterized simply by two constitutive equations: (i) dilatancy,

$$v_y = \psi v_x, \tag{2.4}$$

where ψ is the angle of dilatancy, and (ii) friction,

$$\begin{array}{lrcl} \text{either} & v_x & = & 0 \quad \text{and} \quad |\tau_x| < \mu_0 \tau_y, \\ \text{or} & \tau_x & = & -\mu(v_x)\tau_y \quad \text{and} \quad v_x \geq 0, \end{array} \tag{2.5}$$

where $\mu(v_x)$ is a rate-softening coefficient of friction,

$$\mu(v_x) = \mu_0 [1 - a \sinh^{-1}(v_x / 2 v_{\text{ref}})], \tag{2.6}$$

TABLE 2.1
Parameter values in the model.

Parameter	Definition	Units	Plausible values	Values used in computations
a	Rate-dependence coefficient in friction rule	—	0 — 0.05	0.02, 0.04
D	Hydraulic diffusivity of soil	m^2/s	10^{-8} — 1	10^{-8} — 3×10^{-1}
g	Acceleration of gravity	m/s^2	9.8	9.8
H_s	Thickness of soil block	m	0.1 — 100	0.65
H_w	Height of water table	m	0 — 100	0.3701
K	Hydraulic conductivity of soil	m/s	10^{-11} — 1	2×10^{-9} — 2×10^{-1}
v_{ref}	Reference slip rate in friction rule	m/s	10^{-4} — 1	7×10^{-4} — 4×10^{-1}
θ	Slope angle	radians	0.1 — 0.8	0.5411
μ_0	Static friction coefficient of soil	—	0.2 — 1.2	0.8693
ρ_w	Mass density of pore water	kg/m^3	900 — 1100	1000
ρ_s	Bulk density of dry soil	kg/m^3	1000 — 2200	1600
ϕ	Porosity of soil block	—	0.2 — 0.6	0.4
ψ	Dilatancy angle of shearing soil	radians	-0.2 — 0.2	0.1047

v_{ref} being a reference velocity. Regarding dilatancy, we take ψ to be constant. Under continued shearing, ψ will in fact converge to zero as the soil tends to a critical state. However, as shown in the landslide experiments of [6], the evolution to critical state occurs only when displacement magnitudes greatly exceed those appearing during the processes considered here. Equation (2.6) is a three-parameter representation of rate-weakening friction that we use instead of a more complicated, rate-and-state friction model, which typically employs six parameters. Because of its simplicity, we are able to explore the full relevant parameter space. However, investigation of the model with a rate-and-state friction law remains a task for future research.

Finally, the system is completed by Newton's equations of motion for the block. For this system, the mass per unit area of slope is $\rho_s H_s + \phi\rho_w H_w$. Thus, for the tangential component of the motion we have

$$(\rho_s H_s + \phi\rho_w H_w)\partial_t v_x = (\rho_s H_s + \phi\rho_w H_w) g \sin\theta + \tau_x. \tag{2.7}$$

Regarding the normal component, we are assuming the dilatancy ψ is small, and therefore, in light of (2.4), we may neglect acceleration in the y-direction; thus Newton's equation reduces to force balance. According to Terzaghi's effective-stress principle (e.g., see [2]), the effective normal traction exerted by the slope on the solid matrix is the total stress reduced by the pore pressure at the base; in symbols,

$$\tau_y = (\rho_s H_s + \phi\rho_w H_w) g \cos\theta - p_{\text{tot}}(0,t).$$

On substitution of (2.1), we obtain our last equation,

$$\tau_y = [\rho_s H_s - (1-\phi)\rho_w H_w] g \cos\theta - p_{\text{ex}}(0,t). \tag{2.8}$$

This formulation differs from that of Iverson [5] in two main respects:

- Most importantly, here we allow for rate-softening friction.
- Our assumptions on the imposed pore pressure are more restrictive: specifically, in the notation of (8) of Iverson [5], we assume that $\beta = \cos\theta$ and $W = 0$. Physically, these assumptions imply that there is no flux of groundwater normal to the water table, except for the flux caused by shear-zone dilation.

Provided

$$(\rho_s H_s + \phi\rho_w H_w)\sin\theta \le \mu_0\left[\rho_s H_s - (1-\phi)\rho_w H_w\right]\cos\theta, \tag{2.9}$$

the above equations have a solution with $p_{\text{ex}} = 0$ and $v = 0$: i.e., friction is sufficient to resist the pull of gravity. We study the case where (2.9) is violated.

2.2. Nondimensionalization. We nondimensionalize (2.2)–(2.8) by defining

$$t = \frac{t^{(\text{dim})}}{H_w^2/D}, \quad y = \frac{y^{(\text{dim})}}{H_w}, \quad v = \frac{v_x^{(\text{dim})}}{K}, \quad p = \frac{p_{\text{ex}}^{(\text{dim})}}{\rho_w g H_w}, \quad \tau = \frac{\tau^{(\text{dim})}}{\rho_s g H_s}, \tag{2.10}$$

where the superscript *dim* indicates the dimensional version of a variable. We will eliminate $v_y^{(\text{dim})}$ from the equations, so we do not define a scaled version of this variable; however, we nondimensionalize both components of τ. As in Iverson [5], we have used the diffusive time scale to nondimensionalize t; however, our nondimensionalization of v differs from that of [5]. We also define two dimensionless constants that will appear in the nondimensionalized equations below,

$$\varepsilon = \frac{K/g}{H_w^2/D} \qquad \text{and} \qquad M = \frac{\rho_w H_w}{\rho_s H_s}. \tag{2.11}$$

The first, which according to Table 2.1 is very small, is the ratio of the acceleration time scale to the diffusive time scale; the second is ϕ^{-1} times the ratio of fluid mass to solid mass.

The evolution of the nondimensionalized pressure is governed by

$$\begin{array}{llcll} \text{(a)} & \partial_t p & = & \partial_{yy} p, & 0 < y < 1, \\ \text{(b)} & p(1,t) & = & 0, & \\ \text{(c)} & \partial_y p(0,t) & = & \psi v(t). & \end{array} \tag{2.12}$$

In nondimensional variables, the friction relation (2.5) does not change, except that the rate-softening coefficient in (2.6) must be rescaled to give

$$\mu(v) = \mu_0\left[1 - a\sinh^{-1}\left(\frac{K}{2v_{\text{ref}}}v\right)\right]. \tag{2.13}$$

Newton's equations for the motion of the block scale to

$$\begin{array}{llcl} \text{(a)} & \varepsilon\,\partial_t v & = & \sin\theta - (1+\phi M)^{-1}\tau_x, \\ \text{(b)} & \tau_y & = & [1-(1-\phi)M]\cos\theta - M p_{\text{ex}}(0,t). \end{array} \tag{2.14}$$

In nondimensional variables, the no-motion condition (2.9) may be rewritten as

$$\tan\theta \le A_1\mu_0, \tag{2.15}$$

where A_1 is the first of two mass ratios defined in (2.17) below. If (2.15) is violated and hence $v > 0$, then (2.5) and (2.14)(b) may be combined to solve for τ_x. On substitution into (2.14)(a), we obtain

$$\varepsilon\,\partial_t v = \sin\theta - \mu(v)\left(A_1\cos\theta - A_2 p(0,t)\right), \tag{2.16}$$

where

$$A_1 = \frac{1-(1-\phi)M}{1+\phi M}, \qquad A_2 = \frac{M}{1+\phi M}. \tag{2.17}$$

As long as $v > 0$, the motion is described by (2.12), (2.16).

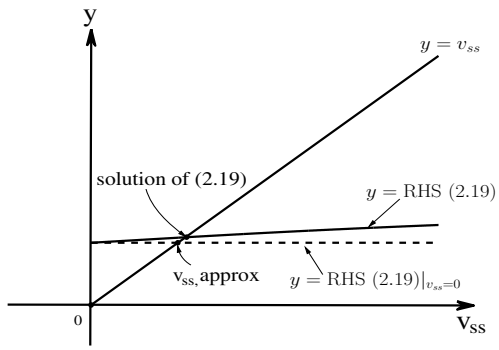

FIG. 2.2. *Graphical solution of* (2.19).

2.3. A steady solution and linearization of the equations. Henceforth we assume that

$$(2.15) \text{ is violated and } \psi > 0.$$

Let us look for a steady-state solution $p_{ss}(y), v_{ss}$ of the equations of motion. It follows from (2.12) that

$$p_{ss}(y) = \psi v_{ss}(y-1), \tag{2.18}$$

and this relation may be substituted into (2.16) to obtain an implicit equation for v_{ss},

$$v_{ss} = (A_2\psi)^{-1}\left[\frac{\sin\theta}{\mu(v_{ss})} - A_1\cos\theta\right]. \tag{2.19}$$

If the friction coefficient is independent of velocity, then this equation is in fact a formula for v_{ss}. Even with rate-softening friction, for parameter values such as in Table 2.1, the right-hand side (RHS) of (2.19) is a slowly varying function of v_{ss} (see Figure 2.2). For example, defining

$$v_{ss,\text{approx}} = (A_2\psi)^{-1}\left[\frac{\sin\theta}{\mu_0} - A_1\cos\theta\right] \tag{2.20}$$

as the solution of (2.19) in the rate-independent case, we may see that

$$\frac{\mu(v_{ss,\text{approx}})}{\mu_0} = 1 - \mathcal{O}\left(\frac{a}{\psi}\frac{K}{v_{\text{ref}}}\right),$$

and, unless ψ is extremely small, we have

$$\frac{a}{\psi}\frac{K}{v_{\text{ref}}} \ll 1. \tag{2.21}$$

Thus, assuming $\psi > 0$ is not too small, we conclude that (2.19) has a unique solution close to $v_{ss,\text{approx}}$.

Incidentally, there is a second solution of (2.19) at very large values of v_{ss}. To see this, observe from (2.13) that $\mu(v)$ vanishes when $v \approx (v_{\text{ref}}/K)e^{1/a}$. Since $\mu(v_{ss})$ occurs

in the denominator, the RHS of (2.19) blows up as v tends to $(v_{\text{ref}}/K)e^{1/a}$, giving rise to a second intersection with the linear function on the left-hand side (LHS). This second steady-state solution of (2.19), for which the velocity is very large indeed, is always unstable, but it can be involved in the steady-state bifurcation of (2.12), (2.16) at extreme parameter values. For clarity, we shall refer to the first solution, given approximately by (2.20), as the *physical* steady state. Referring to the figure and comparing the derivatives of both sides of (2.19), we conclude that at the physical steady state

$$\frac{\sin\theta\,|\mu'(v_{\text{ss}})|}{A_2\psi\,\mu^2(v_{\text{ss}})} < 1. \tag{2.22}$$

To linearize (2.12), (2.16) near the (physical) steady-state solution, we define incremental variables $\overline{p}, \overline{v}$ by

$$p(y,t) = p_{\text{ss}}(y) + \overline{p}(y,t), \qquad v(t) = v_{\text{ss}} + \overline{v}(t).$$

Equations (2.12) are already linear, so we find trivially that

$$\begin{array}{llcll} \text{(a)} & \partial_t\overline{p} & = & \partial_{yy}\overline{p}, & 0<y<1, \\ \text{(b)} & \overline{p}(1,t) & = & 0, & \\ \text{(c)} & \partial_y\overline{p}(0,t) & = & \psi\overline{v}(t), & \end{array} \tag{2.23}$$

and on linearizing (2.16) and simplifying using (2.19) we obtain

$$\varepsilon\partial_t\overline{v} = B_1\overline{p}(0,t) + B_2,\overline{v}, \tag{2.24}$$

where

$$B_1 = A_2\,\mu(v_{\text{ss}}) \quad \text{and} \quad B_2 = \sin\theta\,|\mu'(v_{\text{ss}})|/\mu(v_{\text{ss}}). \tag{2.25}$$

Since $\mu'(v_{\text{ss}}) < 0$, we have used the absolute value to emphasize that $B_2 > 0$.

3. Derivation of the eigenvalue equation. We seek a solution of the linearized equations (2.23), (2.24) with exponential time dependence $e^{-\lambda t}$ (note the minus sign). Using separation of variables, we derive from (2.23)(a),(b) that

$$\overline{p}(y,t) = P\sin[\sqrt{\lambda}(1-y)]e^{-\lambda t}, \qquad \overline{v}(t) = Ve^{-\lambda t},$$

where P and V are constants. Substitution of these formulas into (2.23)(c), (2.24) yields the 2×2 homogeneous linear system

$$\begin{bmatrix} \sqrt{\lambda}\cos\sqrt{\lambda} & \psi \\ B_1\sin\sqrt{\lambda} & \varepsilon\lambda + B_2 \end{bmatrix}\begin{bmatrix} P \\ V \end{bmatrix} = 0. \tag{3.1}$$

This system has a nonzero solution if and only if the determinant of the coefficient matrix vanishes, which leads to the trancendental equation for the decay rate λ,

$$\frac{\tan\sqrt{\lambda}}{\sqrt{\lambda}} = \varepsilon C_1\lambda + C_2, \tag{3.2}$$

where

$$C_1 = 1/B_1\psi, \qquad C_2 = B_2/B_1\psi. \tag{3.3}$$

Recalling (2.25), (2.22), we see that

$$C_2 < 1. \tag{3.4}$$

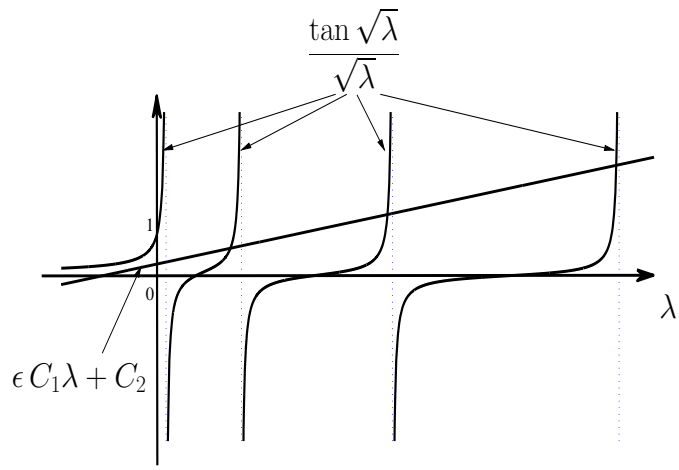

FIG. 4.1. *Graphical determination of the real solutions of* (3.2). *In the figure shown,* $\varepsilon C_1 = 0.02$ *and* $C_2 = 0.3$. *As indicated by* (4.9), *the two complex solutions of* (3.2) *lie in the unstable half-plane,* $\{\mathrm{Re}\,\lambda < 0\}$.

4. Analysis of the eigenvalue equation.

4.1. Introduction. As illustrated in Figure 4.1, (3.2) has an infinite sequence of positive roots. Since these eigenvalues are all in the stable half plane, they do not require further attention. It is not obvious, but (3.2) has two other, possibly complex, roots, which are the focus of the present section.

As a function of a complex variable, $(\tan\sqrt{\lambda})/\sqrt{\lambda}$ is a meromorphic function: i.e., apart from a sequence of poles on the positive real axis, it is single-valued and analytic in the entire plane. Although neither the numerator nor the denominator of this expression is single-valued, the quotient avoids this difficulty. Of course, we use the same branch of $\sqrt{\lambda}$ in the numerator and the denominator so that

$$\lim_{\lambda\to 0}\frac{\tan\sqrt{\lambda}}{\sqrt{\lambda}} = 1.$$

To be specific, let us choose the branch

$$\sqrt{\lambda} = |\lambda|^{1/2}\, e^{i(\arg\lambda)/2}, \tag{4.1}$$

where $\arg\lambda$ satisfies

$$0 \le \arg\lambda < 2\pi.$$

The analysis of the complex roots of (3.2) is based on the simple behavior of $\tan\sqrt{\lambda}$ away from the positive real axis, as articulated in the following proposition.

PROPOSITION 4.1. *Let* Λ *be a wedge in* $\mathbb{C}$ *excluding the positive real axis, say,*

$$\Lambda = \{\lambda \in \mathbb{C} : \delta < \arg\lambda < 2\pi - \delta\}, \tag{4.2}$$

where $0 < \delta < \pi/2$. *Then, as* $|\lambda| \to \infty$ *in* Λ,

$$\tan\sqrt{\lambda} = i + \mathcal{O}(e^{-\delta\sqrt{|\lambda|}/2}). \tag{4.3}$$

Proof. By manipulating the definition of $\tan z$, we deduce that

$$\tan z = i\,\frac{1-e^{2iz}}{1+e^{2iz}}. \tag{4.4}$$

Now $|e^{2iz}| = e^{-2\,\mathrm{Im}\,z}$, so taking $z=\sqrt{\lambda}$ we see that

$$\tan\sqrt{\lambda} = i + \mathcal{O}(e^{-2\,\mathrm{Im}\,\sqrt{\lambda}}).$$

By (4.1), $\mathrm{Im}\,\sqrt{\lambda} = |\lambda|^{1/2}\sin(\arg\lambda/2)$. To complete the proof, we estimate $\arg\lambda$ with (4.2) and use the fact that $\sin(\delta/2)\geq\delta/4$. ∎

4.2. The rate-independent case ($C_2 = 0$). When friction is independent of velocity, the coefficient C_2 in (3.2) vanishes. In the appendix we prove that in this case (3.2) has no zeros in the left half plane: i.e., the steady solution is stable. Since the proof sheds little light on the Hopf bifurcation, we do not include it here. It is instructive, however, to locate the two complex eigenvalues.

Suppose $C_2 = 0$. By (4.3), for large $|\lambda|$ away from the positive real axis, (3.2) may be rewritten, approximately, as

$$e^{i[\pi-\arg\lambda]/2} = \varepsilon C_1|\lambda|^{3/2}e^{i\arg\lambda}.$$

Equating magnitudes we find that $|\lambda| = (\varepsilon C_1)^{-2/3}$, and then equating arguments we find the two approximate roots of (3.2):

$$\lambda = e^{i\pi/3}(\varepsilon C_1)^{-2/3}, \quad e^{5i\pi/3}(\varepsilon C_1)^{-2/3}. \tag{4.5}$$

By (4.3) the error in this estimate is exponentially small in ε. Since $\mathrm{Re}\,\lambda \gg 1$, the associated eigenfunctions decay rapidly in time.

4.3. The rate-dependent case: Steady-state bifurcation. If C_2 assumes positive values, the complex[2] eigenvalues (4.5) can cause the linearized equations (2.23), (2.24) to lose stability if they cross into the left half plane. As we shall see in the next subsection, for physical parameter values, (2.23), (2.24) lose stability through a Hopf bifurcation: i.e., the complex eigenvalues cross the imaginary axis as a pair of complex conjugates. However, for mathematical completeness, we also ask when real solutions of (3.2) cross the imaginary axis. Indeed, one may see by inspection that $\lambda = 0$ is a root of (3.2) iff $C_2 = 1$. If one forces C_2 to its limiting value unity (cf. (3.4)), then the two solutions of (2.19) merge and annihilate one another at a steady-state bifurcation of limit-point type [3].

4.4. The rate-dependent case: Hopf bifurcation.

(a) *Main calculations.* Figure 4.2 shows a curve Γ in the $(\varepsilon C_1, C_2)$-plane that separates the infinite strip

$$\{(\varepsilon C_1, C_2)\ :\ 0<\varepsilon C_1<\infty,\ 0<C_2<1\}$$

into two regions in which (2.23), (2.24) are stable or unstable. This curve has the parametric representation

$$\varepsilon C_1 = \frac{2}{\mu^3}\,\frac{1-2e^{-\mu}\sin\mu - e^{-2\mu}}{1+2e^{-\mu}\cos\mu + e^{-2\mu}}, \tag{4.6}$$

[2]We shall refer to these roots of (3.2) as *complex* eigenvalues even though, for extreme parameter values, they may actually become real.

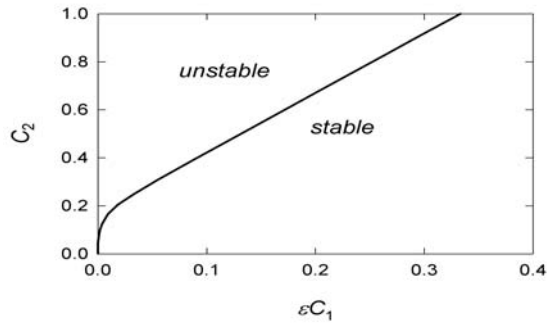

FIG. 4.2. *Graph of the Hopf bifurcation curve* Γ *defined parametrically by* (4.6), (4.7).

$$C_2 = \frac{1}{\mu}\,\frac{1+2e^{-\mu}\sin\mu - e^{-2\mu}}{1+2e^{-\mu}\cos\mu + e^{-2\mu}}, \tag{4.7}$$

where $0 \le \mu < \infty$. In the following proposition we show that (2.23), (2.24) undergo Hopf bifurcation when C_1, C_2 lies on Γ.

PROPOSITION 4.2. *If* $\varepsilon C_1, C_2$ *lie on* Γ, *then the complex eigenvalues of* (3.2) *are pure imaginary.*

Proof. Suppose (3.2) has a root on the positive imaginary axis, say, at $\lambda = i\mu^2/2$, where $\mu \ge 0$. Then $\sqrt{\lambda} = (1+i)\mu/2$. Equating real and imaginary parts of (3.2), we conclude that

$$\varepsilon C_1 = \frac{2}{\mu^2}\,\mathrm{Im}\left\{\frac{\tan[(1+i)\mu/2]}{(1+i)\mu/2}\right\}, \qquad \varepsilon C_2 = \mathrm{Re}\left\{\frac{\tan[(1+i)\mu/2]}{(1+i)\mu/2}\right\}. \tag{4.8}$$

We claim that

$$\tan[(1+i)\mu/2] = \frac{2e^{-\mu} + i(1-e^{-2\mu})}{1+2e^{-\mu}\cos\mu + e^{-2\mu}},$$

which may be proved by recalling (4.4), multiplying and dividing by the complex conjugate of the denominator, and simplifying. Equations (4.6), (4.7) result on multiplying by $[(1+i)\mu/2]^{-1} = (1-i)/\mu$ and substituting into (4.8). ∎

By examining the Taylor series expansions of the numerators in (4.6), (4.7), we see that

$$\lim_{\mu\to 0} \varepsilon C_1 = 1/3, \qquad \lim_{\mu\to 0} C_2 = 1,$$

which is behavior that may be seen in Figure 4.2. At the other extreme, $\mu \gg 1$, or equivalently $\varepsilon C_1 \ll 1$, the exponentials in (4.6), (4.7) may be neglected, so that it is possible to eliminate μ and obtain a relation between the C's that characterizes Hopf bifurcation:

$$C_2 = \left(\frac{\varepsilon C_1}{2}\right)^{1/3}, \tag{4.9}$$

both sides of the equation being small. The proof of the proposition shows that at parameter values given by (4.6), (4.7), the complex eigenvalues of (2.23), (2.24)

are $\pm i\mu^2/2$, and in the asymptotic range the complex eigenvalues are approximately $\pm iC_2^{-2}/2$. In particular, the bifurcating periodic solutions have periods approximately equal to

$$\frac{2\pi}{|\lambda|} \approx 4\pi C_2^2. \tag{4.10}$$

Our simulations below confirm the accuracy of this prediction.

It is natural to undo the nondimensionalization of the equations to seek a prediction for the period of oscillations of landslide motion in the field. However, the enormous ranges of D, K, and v_{ref} in Table 2.1 diminish the value of this exercise. Specifically, one obtains oscillation periods ranging from about 10^{-7} to 10^3 seconds. At the small end, these periods will be unobservable by conventional measurement techniques. At the upper end, these periods are similar to those sometimes observed in the field and also observed in the landslide experiments of Iverson et al. [6].

(b) *Numerical limitations.* Provided $\varepsilon C_1 \ll 1$, (4.9) characterizes the loss of stability in the PDE (2.23), (2.24) through Hopf bifurcation. However, this relation is not accurate for numerical simulations if

$$\varepsilon C_1 \leq \mathcal{O}(h^3), \tag{4.11}$$

where h is the mesh size. To motivate this assertion, first recall that the eigenvalues of the PDE at the bifurcation point have absolute value

$$\mu^2/2 = 1/(2C_2^2) = 2^{-1/3}(\varepsilon C_1)^{-2/3} \gg 1.$$

On the other hand, the largest eigenvalue of the discretization is $\mathcal{O}(h^{-2})$, and moreover the large eigenvalues of the discretization do not approximate eigenvalues of the PDE. These two observations warn of a mismatch if

$$(\varepsilon C_1)^{-2/3} \geq \mathcal{O}(h^{-2}),$$

which is equivalent to (4.11).

Let us illustrate this phenomenon for a second-order explicit discretization of the PDE. (In the simulations below, we used the Crank–Nicholson method, for which the analysis is similar in spirit but more technical in detail.) For a positive integer N, let $h = 1/N$ be the mesh size in discretizing space, and let

$$y_n = 1 - nh, \quad n = 0, 1, \ldots, N+1.$$

Consider the semidiscrete approximation for the pressure equation (2.23),

(4.12)

$$\begin{array}{lrcll} \text{(a)} & \partial_t p_n & = & h^{-2}\left[p_{n+1} - 2p_n + p_{n-1}\right], & n = 1, 2, \ldots, N, \\ \text{(b)} & p_0 & = & 0, & \\ \text{(c)} & (2h)^{-1}\left[p_{N-1} - p_{N+1}\right] & = & \psi v, & \end{array}$$

and for the velocity equation (2.24),

$$\varepsilon \partial_t v = B_1 p_N + B_2 v. \tag{4.13}$$

As with the PDE, we look for solutions of (4.12), (4.13) such that $p_n(t)$ and $v(t)$ have exponential time dependence $e^{-\lambda t}$. It follows from (4.12)(a),(b) that

$$p_n(t) = Pe^{-\lambda t}(z^n - z^{-n}), \qquad n = 0, 1, \ldots, N+1,$$

$$v(t) = Ve^{-\lambda t},$$

where

$$\lambda = \frac{z - 2 - z^{-1}}{h^2}. \tag{4.14}$$

Substituting into (4.12)(c), (4.13), we obtain a solution provided

$$\det \begin{bmatrix} (2h)^{-1}(z - z^{-1}) & \psi \\ B_1 & B_2 - \varepsilon h^{-2}(z - 2 - z^{-1}), \end{bmatrix} = 0, \tag{4.15}$$

where we have divided the first column of this determinant by z^N.

We analyze the Hopf bifurcation in this system as with the PDE: i.e., we ask when there is a solution z of (4.15) such that λ, computed according to (4.14), lies on the imaginary axis, say, $\lambda = i\mu$. We consider only the asymptotic range $\mu \gg 1$. Hence $z \gg 1$, and we may solve (4.14) for z approximately by neglecting z^{-1}; i.e.,

$$z = 2 + i\mu h^2.$$

Substituting this approximation into (4.15) and solving for B_i from (3.3), we rewrite (4.15) as

$$\det \begin{bmatrix} h^{-1} + i\mu h/2 & \psi \\ 1/(\psi C_1) & C_2/C_1 - i\varepsilon\mu \end{bmatrix} = 0. \tag{4.16}$$

From the vanishing of the imaginary part of this equation, we conclude that

$$C_2 = \frac{2}{h^2}\,\varepsilon C_1, \tag{4.17}$$

which is the relation that characterizes Hopf bifurcation at large eigenvalues in the discretization; thus, (4.17) replaces (4.8) when discretization effects invalidate the latter.

5. Supporting computations.

5.1. Methods. To test our bifurcation predictions and examine details of the dynamics described by (2.2) and (2.7), we solved discretized versions of the equations numerically. Values of most parameters used in the computations were fixed to match those of physical landslide experiments in which both quasi-steady sliding and stick-slip behavior were observed [6], whereas values of K, D, and v_{ref} were modified systematically to make computational transects of the εC_1-C_2 parameter space (Table 2.1). Specifically, values of ε were manipulated by adjusting the values of K and D in accordance with values appropriate for diverse soils; then, while holding εC_1 essentially constant, C_2 was increased incrementally through a plausible range by adjusting v_{ref}. As C_2 increased, bifurcation was detected as a transition from convergent oscillations (leading to a stable steady state) to divergent oscillations (leading to repetitive stick-slip cycles) in the v-p phase plane, a result described in more detail below.

With few exceptions, the value of the rate-weakening friction parameter a used in all computations was 0.02, consistent with observations in rate-controlled shear tests with many soil-like materials [8, 12]. To attain values of C_2 large enough to cause bifurcation when $\varepsilon C_1 > 0.1$, however, it was necessary to increase a to 0.04. Such

large values of a, C_2, and εC_1 are atypical and perhaps even physically implausible, but mathematically they characterize the upper fringes of the εC_1-C_2 parameter space.

Our computational algorithm employed an explicit fourth-order Runge–Kutta method to solve the ODE (2.7) and the Crank–Nicholson method to solve the PDE (2.2) [9] in an operator-splitting scheme. First a Runge–Kutta time step Δt was taken to advance the slide-block velocity $v_x(t)$ while holding the excess basal pore pressure $p_{\text{ex}}(0,t)$ constant; then using the new $v_x(t)$ to update the basal boundary condition (2.3b) a Crank–Nicholson time step Δt was taken to advance the pore-pressure diffusion solution $p_{\text{ex}}(y,t)$. The updated pore-pressure solution provided the basal pore pressure necessary to take the next Runge–Kutta step. Refinement of this scheme by using the mean $v_x(t)$ between successive time steps to update (2.3b) and then recompute $p_{\text{ex}}(y,t)$ using this mean yielded solutions that differed negligibly from those of the basic scheme, provided that time steps were sufficiently small. Therefore, we used the basic scheme for all computations reported in this paper.

Our discretization of (2.2) and (2.7) used times steps with a size Δt suitable for resolving slide-block acceleration, which had an intrinsic timescale K/g typically much smaller than that of pore-pressure diffusion (i.e., $\varepsilon \ll 1$). In trial calculations we initially set $\Delta t = (K/g)\sin\theta$, the time necessary for the block to accelerate from 0 to K in the absence of friction and pore-pressure feedback. Subsequent trials showed that when friction and feedback were present, $\Delta t \gg (K/g)\sin\theta$ could generally be used with negligible loss of accuracy. Therefore, we consistently employed $\Delta t = 0.0002s$ to produce all computational results reported in this paper, although we regularly checked these results against those obtained using smaller time steps. Also, for the sake of consistency, our spatial discretization of (2.2) employed $h = 0.001$ for all results reported here, except for trials exploring finite-h effects.

In all computations we used $H_w = 0.3701m$, a value 1% larger than the static limiting equilibrium value that applies when (2.9) reduces to an equality for the parameter values listed in Table 2.1. As indicated by (2.1), fixing the initial value of H_w also fixed the background pore-pressure distribution $p_{\text{hydro}}(y)$. An initial excess pore-pressure distribution could be specified by (2.18), using (2.20) as an estimate for the steady-state velocity. In practice, during production runs, we iterated (2.19) one or more times to improve the initial estimate (2.20), in order to hasten convergence to the steady state.

5.2. Results. Our computational results are summarized in Figure 5.1, a graph that depicts theoretical bifurcation curves and computed bifurcation points in the εC_1-C_2 parameter space. The broad range of values spanned by this parameter space reflects the broad range of K and D values that are physically plausible for diverse soils (e.g., [2]), and it illustrates the wide scope of the bifurcation phenomenon.

We determined all bifurcation points shown in Figure 5.1 to at least two significant digits. At this level of precision, the computed bifurcation points lie exactly on the theoretical Hopf-bifurcation curve Γ (solid line in Figure 5.1), provided the simulation is not polluted by finite-h effects. When $\varepsilon C_1 \leq \mathcal{O}(h^3)$, numerical effects determine the location of the bifurcation point, and it may be seen from the figure that the bifurcation is accurately described by (4.17) (dashed line in Figure 5.1).

The physical character of the Hopf bifurcation is illustrated by phase portraits depicting coevolution of $v_x(t)$ and $p_{\text{ex}}(0,t)$. Figure 5.2 shows typical phase portraits

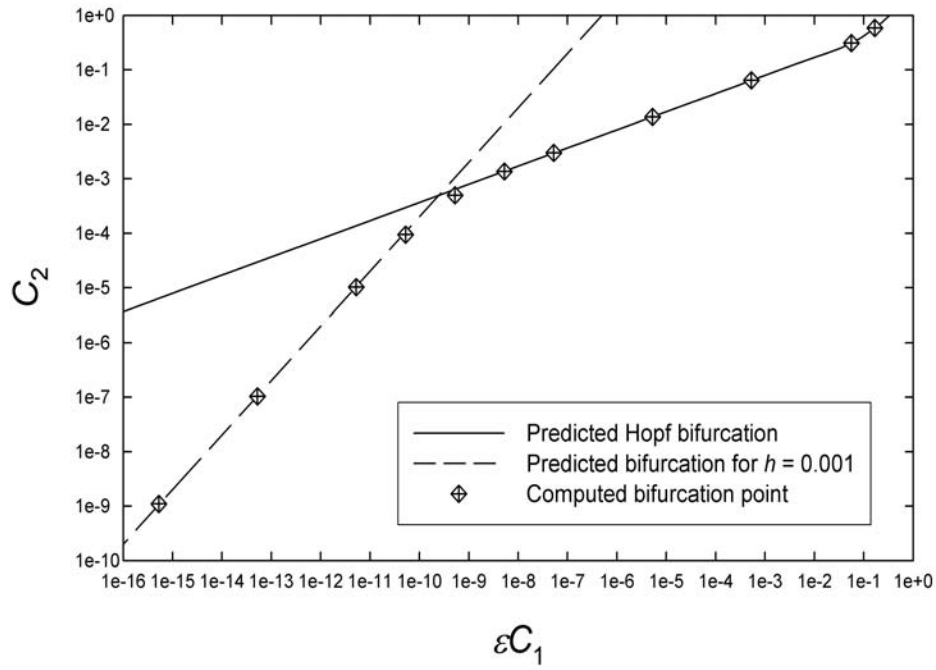

FIG. 5.1. *Comparison of computed bifurcation points with the Hopf bifurcation curve* Γ *predicted by* (4.6), (4.7) *(solid line), and the finite-h limit* (4.17) *for the case in which* $h = 0.001$ *(dashed line).*

for C_2 near the bifurcation point. The bifurcation is subcritical—when $C_2 > C_{2\text{Hopf}}$, the solution evolves to a periodic solution whose amplitude does not tend to zero as $C_2 \to C_{2\text{Hopf}}$. (Note that Figures 5.2B and 5.2C have different scales.) As expected, the evolution toward or away from the steady state slows down as the bifurcation point is approached [11].

For the parameter values used in making Figure 5.2, (4.10) predicts that near the bifurcation point, the period of oscillations is 0.325 s. By comparision, the oscillations depicted in Figure 5.2C have a computed period of 0.336 s. The fairly large discrepancy between these two numbers is related to the fact that the bifurcation is subcritical. Strictly speaking, (4.10) predicts the period of the small-amplitude, unstable orbits close to the bifurcation point, while Figure 5.2C shows a moderate-amplitude, stable orbit to which the solution jumps when C_2 exceeds $C_{2\text{Hopf}}$. A better comparison is provided by the nearly periodic, decaying solution shown in Figure 5.2B, in which the numerically estimated period is 0.324 s.

During part of the periodic orbits in Figures 5.2C and 5.2D, the velocity vanishes. This stick-slip behavior occurs because the nonlinearity limiting growth of the oscillations is a nonsmooth one, i.e., the discontinuous behavior of friction at $v = 0$. In no instance did oscillations persist without stick-slip behavior.

Transitions in phase-portrait behavior for other values of εC_1 were qualitatively similar to those illustrated in Figure 5.2 except for unphysically large values of εC_1: i.e., near the end of Γ at the point $(1/3, 1)$. In the latter case, the large-time orbit differs from Figure 5.2 in that the block "sticks" during a large fraction of the period, even immediately after bifurcation.

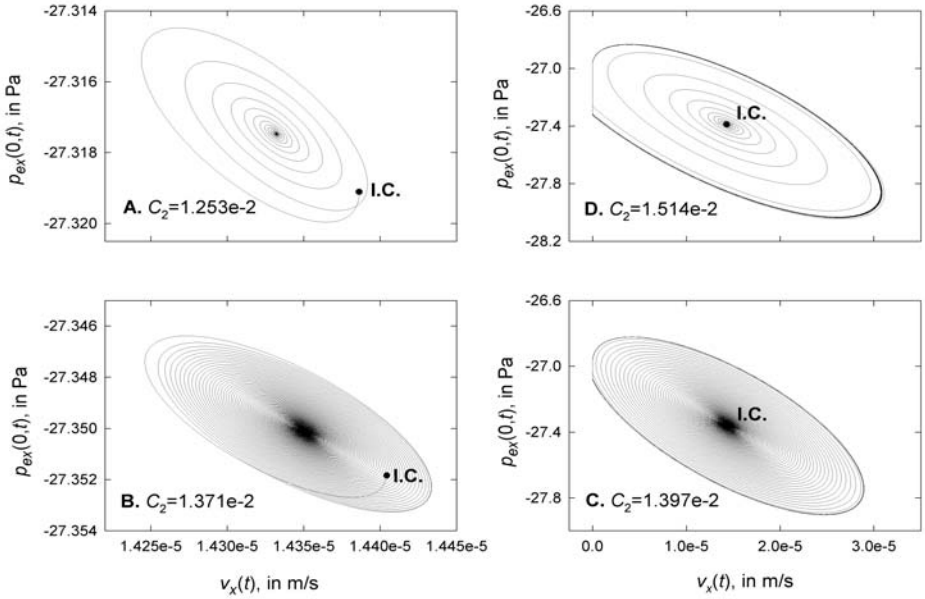

FIG. 5.2. *Examples of computed orbits in the v_x, p_{ex} phase plane for a case in which $\varepsilon C_1 = 5.256\times10^{-6}$ and $C_{2Hopf} = 1.380\times10^{-2}$. These computations used $K = 2\times10^{-4}$ m/s, $D = 1\times10^{-3}$ m^2/s, $a = 0.02$, and values of v_{ref} ranging from 2.4×10^{-3} to 2.9×10^{-3} m/s to obtain varying values of C_2. All other parameters were held fixed at the values listed in Table 2.1. The point marked "I.C." indicates the initial condition used in each computation. Note that the value of C_2 increases moving counterclockwise in the figure from frames* A *through* D. *In frame* B, *C_2 is just below critical, while in frame* C, *it is just above. Incidentally, in frame* D, *motion along the portion of the trajectory where $v \equiv 0$, which is governed by diffusion alone, is slower than along the remainder of the trajectory, and this effect is more pronounced if C_2 is further from the bifurcation point.*

6. Concluding discussion. Hopf bifurcation occurs in solutions of equations that provide a parsimonious model of landslide motion regulated by dilatancy, pore-pressure feedback, and rate-weakening friction. The bifurcation is manifested as an abrupt transition (thus, the bifurcation is subcritical) from stable, steady, downslope motion to periodic motion characterized by repetitive stick-slip cycles. The existence of stick-slip behavior in this system is noteworthy because, unlike classical models that exhibit stick-slip, our model includes no elastic element that exerts a variable and reversible driving force. (The archetype model for stick-slip behavior is a rate-weakening friction block pulled along a plane by an elastic spring.) Instead, in our model, the driving force is the steady pull of gravity, and the frictional resisting force is mediated by pore-pressure diffusion. Effects of pore-pressure diffusion have also been studied in the context of stick-slip models that include an elastic driving element [10], but to our knowledge no previous model has duplicated ours in omitting elastic forces while retaining the capacity for stick-slip behavior.

Analysis and computations show that the Hopf bifurcation leading to stick-slip behavior in our model is precisely governed by the parameters εC_1 and C_2, although decomposition of these parameters into their physical components shows that their variation depends mostly on variations in ε and the velocity ratio $K/v_{\rm ref}$. Physically, the timescale ratio ε specifies the relative speeds at which the landslide characteristically moves and excess pore pressure characteristically diffuses, whereas $K/v_{\rm ref}$

specifies the degree to which rate-weakening friction affects landslide motion. For relevant parameter values (Table 2.1), $\varepsilon \ll 1$ applies almost universally, indicating that pore-pressure diffusion is a relatively slow process that serves to regulate the inherently faster process of landslide motion. Also, for relevant parameter values, $K/v_{\text{ref}} \ll 1$ is typical, although K/v_{ref} values of order 1 or larger are possible (see Table 2.1). For $K/v_{\text{ref}} \ll 1$, the characteristic slip velocity $v_x = \mathcal{O}(K)$ is small. Taking the limit $v_{\text{ss}} = 0$ and then combining (3.3), (2.25), and (2.6), we calculate that

$$C_2 = \frac{\sin\theta}{\psi A_2}\,\frac{aK}{2\mu_0 v_{\text{ref}}},$$

which shows that, for $K/v_{\text{ref}} \ll 1$, increases in K/v_{ref} produce increases in C_2 and hence decreases in stability. This is the behavior typically observed in our computations. By contrast, if K/v_{ref} becomes comparable to or greater than 1, increases in K/v_{ref} can produce decreases in C_2 and hence *increases* in stability. Physically, this behavior reflects the fact that friction, which decreases logarithmically at large velocities, becomes increasingly insensitive to v as slip rates grow large.

Another important observation regarding the physics described by our model concerns the consistent manner in which orbits in the v_x-p_{ex} phase plane are skewed. As shown in Figure 5.2, the minimum $p_{\text{ex}}(0,t)$ always lags the maximum $v_x(t)$ by less than one quarter of an orbit cycle, irrespective of whether orbits diverge unstably or converge to a fixed point. Similar orbit skewness is exhibited in all of our computational results. However, as $\varepsilon C_1 \to 0$ the orbit skewness gradually diminishes, so that orbits become almost symmetrical about the line $v_x = v_{\text{ss}}$ and the phase lag approaches 1/4-cycle. This skewness of the orbits is a consequence of inertia. To illustrate this, observe that $\varepsilon C_1 \to 0$ if, for example, $K \to 0$; it follows from (2.10) that the dimensional steady-state velocity tends to zero as $K \to 0$, and hence inertial effects will disappear in this limit.

Finally, we emphasize that two key effects are not included in our model: (i) parameter evolution (e.g., dilatancy evolution) and (ii) a rate-and-state friction law in which the friction coefficient evolves with time [1, 10]. Such effects could lead to other kinds of instabilities, including a possibly more complex bifurcation than what we have analyzed.

Appendix.

PROPOSITION A.1. *If $C > 0$, the function*

$$f(\lambda) \equiv \frac{\tan\sqrt{\lambda}}{\sqrt{\lambda}} - C\lambda$$

has no zeros in the closed left half plane $\{\lambda : \operatorname{Re}\lambda \le 0\}$.

Proof. For any $R > 0$, let Ω_R be the half disk

$$\{\lambda : \operatorname{Re}\lambda < 0,\ |\lambda| < R\},$$

inside which f is analytic. According the principle of the argument [7, Chapter 4, section 4], provided f is nonzero on $\partial\Omega_R$, the number of zeros of f in Ω_R equals the variation of $\arg f$ around the boundary. It is obvious that $\operatorname{Re}(-C\lambda) \ge 0$ on $\partial\Omega_R$. We claim that, no matter how large R may be,

$$\operatorname{Re}\frac{\tan\sqrt{\lambda}}{\sqrt{\lambda}} > 0 \qquad \text{on } \partial\Omega_R.$$

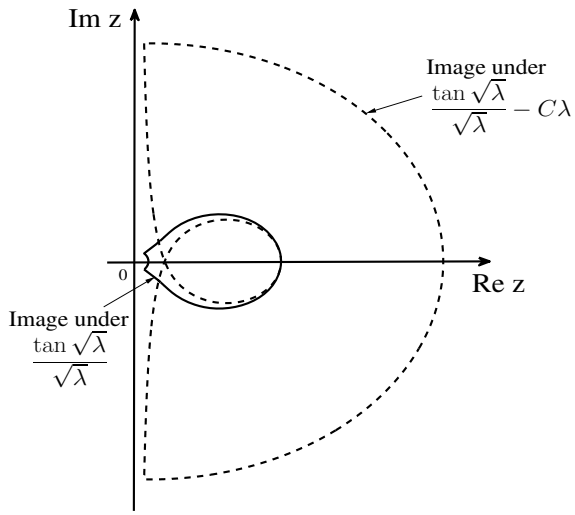

FIG. A.1. *Images of the semicircle $\partial\Omega_R$ in the complex plane under two mappings (see the appendix). The radius $R = 100$, and the constant $C = 0.02$.*

Thus, the variation of the argument of f around $\partial\Omega_R$ is zero, and this proves the result.[3]

Let us prove the claim. For λ on the semicircle $\{\lambda : \operatorname{Re}\lambda \le 0, |\lambda| = R\}$, we invoke the asymptotic form (4.3) and observe that

$$\operatorname{Re}\frac{i}{\sqrt{\lambda}} = |\lambda|^{-1/2}\cos\left(\frac{\pi - \arg\lambda}{2}\right) > 0;$$

the reason for the inequality is that $-\pi/4 \le (\pi - \arg\lambda)/2 \le \pi/4$. For λ on the imaginary axis, since $f(\overline{\lambda}) = \overline{f(\lambda)}$, it suffices to restrict our attention to $\{\operatorname{Im}\lambda \ge 0\}$. Along the nonnegative imaginary axis we may parametrize $\sqrt{\lambda}$ as

$$\sqrt{\lambda} = (1+i)t, \qquad t \ge 0.$$

Substituting into (4.4), we find

$$\frac{\tan\sqrt{\lambda}}{\sqrt{\lambda}} = \frac{i}{(1+i)t}\,\frac{1 - e^{2i(1+i)t}}{1 + e^{2i(1+i)t}}.$$

Multiplying both the numerator and the denominator by the complex conjugate of the denominator and collecting terms, we calculate that

$$\operatorname{Re}\frac{\tan\sqrt{\lambda}}{\sqrt{\lambda}} = p(t)\,\frac{\sinh 2t + \sin 2t}{t} > 0,$$

where the positive factor

$$p(t) = \left|1 + e^{2i(1+i)t}\right|^{-2}$$

comes from the modulus squared of the denominator. This proves the proposition. ∎

[3]The reader may find it interesting to consult Figure A.1, which shows the image of $\partial\Omega_R$ under $(\tan\sqrt{\lambda})/\sqrt{\lambda}$ and under f.

REFERENCES

[1] J. H. Dieterich and B. D. Kilgore, *Direct observation of frictional contacts: New insights for state-dependent properties*, Pure and Applied Geophysics, 143 (1994), pp. 283–302.

[2] R. A. Freeze and J. A. Cherry, *Groundwater*, Prentice-Hall, Englewood Cliffs, NJ, 1979.

[3] M. Golubitsky and D. Schaeffer, *Singularities and Groups in Bifurcation Theory*, *Vol.* I, Springer-Verlag, New York, 1985.

[4] R. M. Iverson, *Dilatancy, pore-pressure feedback, and regulation of landslide (and thrust fault) motion*, Geological Society of America Annual Meeting, Abstracts with Programs, 34 (2003), p. 196.

[5] R. M. Iverson, *Regulation of landslide motion by dilatancy and pore pressure feedback*, J. Geophys. Res., 110 (2005), F02015.

[6] R. M. Iverson, M. E. Reid, N. R. Iverson, R. G. LaHusen, M. Logan, J. E. Mann, and D. L. Brien, *Acute sensitivity of landslide rates to initial soil porosity*, Science, 290 (2000), pp. 513–516.

[7] N. Levinson and R. Redheffer, *Complex Variables*, Holden-Day, San Francisco, CA, 1970.

[8] P. L. Moore, N. R. Iverson, and R. M. Iverson, *Frictional properties of the Mount St. Helens gouge*, Chapter 20 in A Volcano Rekindled: The Renewed Eruption at Mount St. Helens, 2004-2006, D. R. Sherrod, W. E. Scott, and P.E. Stauffer, eds., U.S. Geological Survey Professional Paper 1750, in press.

[9] W. H. Press, B. P. Flannery, S. A. Teukolsky, and W. T. Vettering, *Numerical Recipes*, Cambridge University Press, Cambridge, UK, 1986.

[10] P. Segall and J. R. Rice, *Dilatancy, compaction, and slip instability of a fluid-infiltrated fault*, J. Geophys. Res., 100 (1995), pp. 22155–22172.

[11] S. Strogatz, *Nonlinear Dynamics and Chaos*, Westview Press, Boulder, CO, 1994.

[12] T. E. Tika, P. R. Vaughan, and L. J. Lemos, *Fast shearing of preexisting shear zones in soil*, Geotechnique, 46 (1996), pp. 197–233.